Chapter 6

Characterization and Noise Performance of a Time-Domain Breast Imaging System

A comprehensive characterization of the Time-Domain Breast Imaging System is presented. The knowledge learned from this characterization is applied to the modeling of real data. The noise model presented in Chapter 5 is used to provide a fit to the data, leading to further insight into the system-level performance and methods for optimizing performance in a clinical setting.

6.1 Characterization

First, the spectral response of both the laser system and the camera system are determined. The spectral bandwidth of the laser is then used to estimate the laser pulse width. Warm-up time to steady state is then explored both at the subsystem and system levels. Transient response of the laser to changes in wavelength is characterized next, followed by transient response of the acquisition process itself. The subsystem and system-level stability and repeatability are assessed next. The gain of the ICCD is determined as a function of the MCP gain voltage. Linearity of both the intensifier and the CCD camera are determined. The intensifier is characterized by two types of saturation, both of which have implications on the system performance. The impulse response of the system is explored and explanations for deviations from ideal behavior are provided. The cross talk will be shown to be low and well within the requirements of

this imaging system. This section is completed with an assessment of the dark performance of the ICCD system, which provides further insight into noise character.

6.1.1 Spectral Response of Laser and ICCD

The output spectrum of the Spectra Physics mode-locked Mai-Tai Ti:Sapphire laser is shown in Figure 6.1. The laser is tunable on 1 nm resolution between 750 and 850 nm. The spectral data was collected at the output of one of the probe's source fibers which was coupled to an Ocean Optics S2000 spectrometer. The spectrometer was

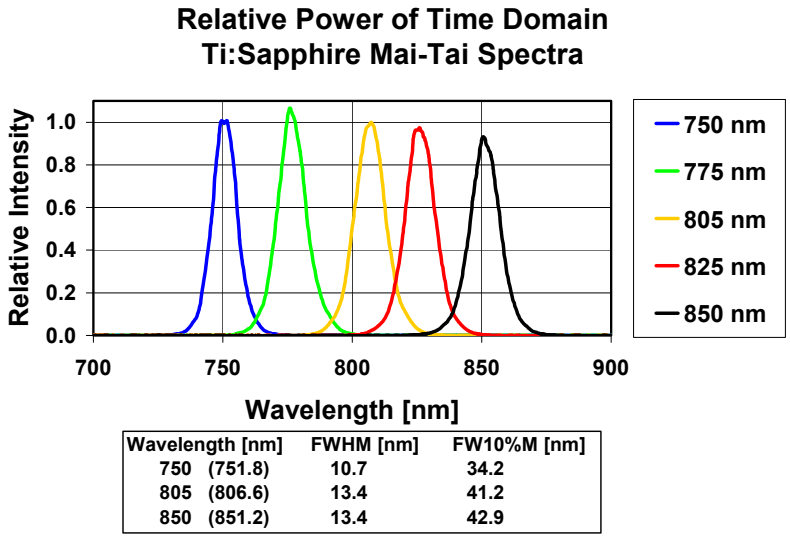

Wavelength [nm]	FWHM [nm]	FW10%M [nm]
750 (751.8)	10.7	34.2
805 (806.6)	13.4	41.2
850 (851.2)	13.4	42.9

Figure 6.1 The relative power and spectral width of the Spectra Physics Mai-Tai Ti:Sapphire mode-locked laser is shown over a spectral range between 750 and 850 nm.

radiometrically calibrated against a NIST traceable tungsten calibration lamp. The spectral width of the laser output at 750 nm was more than 20% lower than at 850 nm, resulting in proportionally lower power when the intensity is integrated over wavelength. The relative response with wavelength shown in Figure 6.2 was collected with a Coherent FieldMaster model FM/GS thermal detector which was also calibrated to NIST traceable

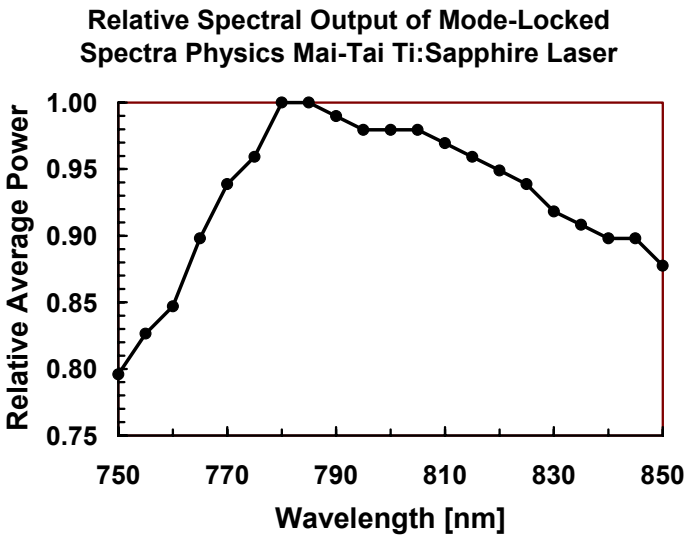

Figure 6.2 The spectral output of the mode-locked Spectra-Physics Mai-Tai Ti:Sapphire laser is shown over the wavelength range between 750 and 850 nm. The absolute power was controlled by the angle of the Glan polarizer relative to the linear polarization angle of the laser output and is adjustable from about 1.5 to 800 mW. The data was collected using a radiometrically calibrated thermal detector as measured at the output of the source probe fiber.

sources. The average laser power is shown to peak in the vacinity of 780 nm, falling off by 20% at 750 and by about 13% at 850 nm.

A simple relationship can be derived between the pulse width and the spectral width of a laser pulse from the well known equation

$$c = \lambda \nu \qquad (6.1)$$

where c is the speed of light in vacuum, λ is the wavelength, and ν is the frequency. Rearranging and taking the derivative with respect to time gives

$$\frac{d\lambda}{dt} = c\frac{d}{dt}\left(\frac{1}{\nu}\right) \qquad (6.2).$$

This can be written in terms of incremental wavelength and frequency as

$$\Delta\lambda = -\frac{c}{\nu^2}\Delta\nu \qquad (6.3).$$

Using the relation

$$\Delta\nu = \frac{1}{\Delta t} \tag{6.4}$$

and using Equation 6.1 to substitue for ν in Equation 6.3, gives

$$\Delta\lambda = -\frac{\lambda^2}{c}\frac{1}{\Delta t} \tag{6.5}$$

which allows the approximate pulse widths of the laser to be determined. This relation gives a pulse width of 200 femtoseconds for 750 nm and 160 femtoseconds for both 805 and 850 nm.

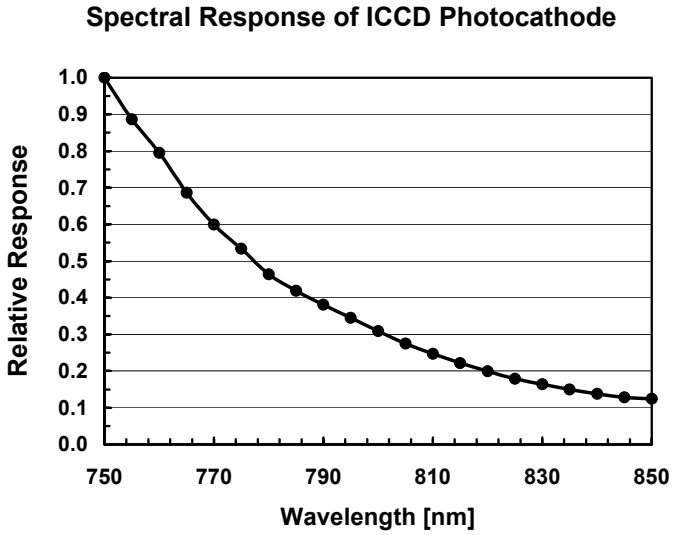

Figure 6.3 The spectral response of the La Vision ICCD photocathode is shown over the response range of the Ti:Sapphire laser. The data was acquired by the use of a radiometrically calibrated thermal detector as a calibration for the incident flux.

The radiometrically calibrated Ti:Sapphire laser ouptut was used as input to the camera system to determine the spectral response of the photocathode as shown in Figure 6.3. The response varies significantly between 750 and 850 nm dropping to only 12%. The photocathode material is specified as S20, which has a quantum efficiency on the order of 3.8% at 750 nm, peaking at close to 10% in the blue-green around 500 nm. The much greater sensitivity of the photoocathode to the visible spectrum relative to the near

infrared region where we are interested, suggests that it would be prudent to include a bandpass or longpass interference filter to attenuate unwanted background photons from ambient light conditions, as described in Chapter 5. Other photocathode materials are available, such as the extended red version of the S20, referred to as the S25 photocathode. Photocathode materials such as the NEA semiconductors mentioned in Chapter 5, based on GaAs may offer some advantage in the near infrared, but were not available from the manufacturer. Generally, the quantum yields of the photocathode materials that extend further into the near infrared are low and exhibit higher noise relative to the classical materials such as S20, so care should be exercised in not jumping to the conclusion that they will offer superior performance, unless one is interested in detection beyond 900 nm, where the classical emitter bandgaps result in essentially no response.

6.1.2 Warm-Up Time

It is important to understand the time required for the complete Time-Domain Breast Imaging System to reach steady state thermal equilibrium, which is described as warm-up time. Any measurements made prior to this time are subject to drift in system response that may result in errors in the reconstructed data. Figure 6.4 shows the results of testing the warm-up response of the laser, Multiplexer, and ICCD independently. In each case the subsystem under test was only started after the balance of the subsystems were allowed a period of 3 hours to thermally equilabrate. Both the Multiplexer and the ICCD were shown to reach to within 0.2% of their asymptotic values within a 30 minute period. The laser required a period of about 60 minutes to reach the same level. If it is

acceptable to be within 1% of the final value for the system, then only on the order of 15 to 20 minutes is required for all subsystems taken together. For any given measurement, it is only the drift which occurs within the measurement period that is important, so with

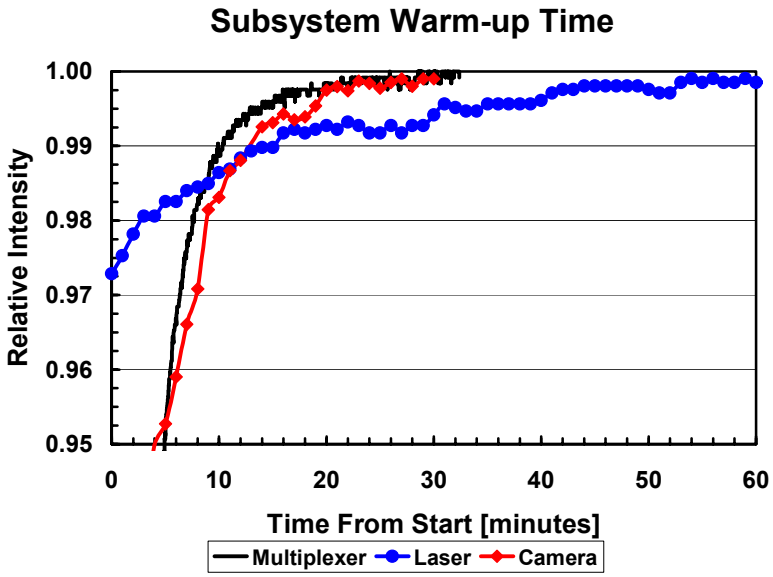

Figure 6.4 The transient warm-up responses of the custom fiber optic laser source Multiplexer, the Spectra-Physics Mai-Tai mode-locked laser, and the La Vision PicoStar HR ICCD camera are shown. In each case, the other two subsystems were warmed up for a period of 3 hours prior to turn-on of the subsystem under test to assure that only the response of that subsystem was responsible for the transient response indicated.

that in mind it is the slope of the warm up transient response that is of importance. With that perspective, the system should be measurement-ready by within 20 minutes from start-up. The Spectra Physics laser requires approximately 20 to 30 minutes to pre-warm-up prior to turning on the pump diodes in the laser head. The warm-up time is in addition to this pre-warm-up time. Thus the limiting subsystem would necessarily be the laser, as both the multiplexer and the camera warmed up within the time period required for laser pre-warm-up.

A look at the full TPSF's provides further insight into warm-up phenomenon as shown in Figure 6.5. Plot (A) of Figure 6.5 shows the unshifted TPSF's for the three trials of Figure 6.5 for a source fiber located in the center of the source face of the

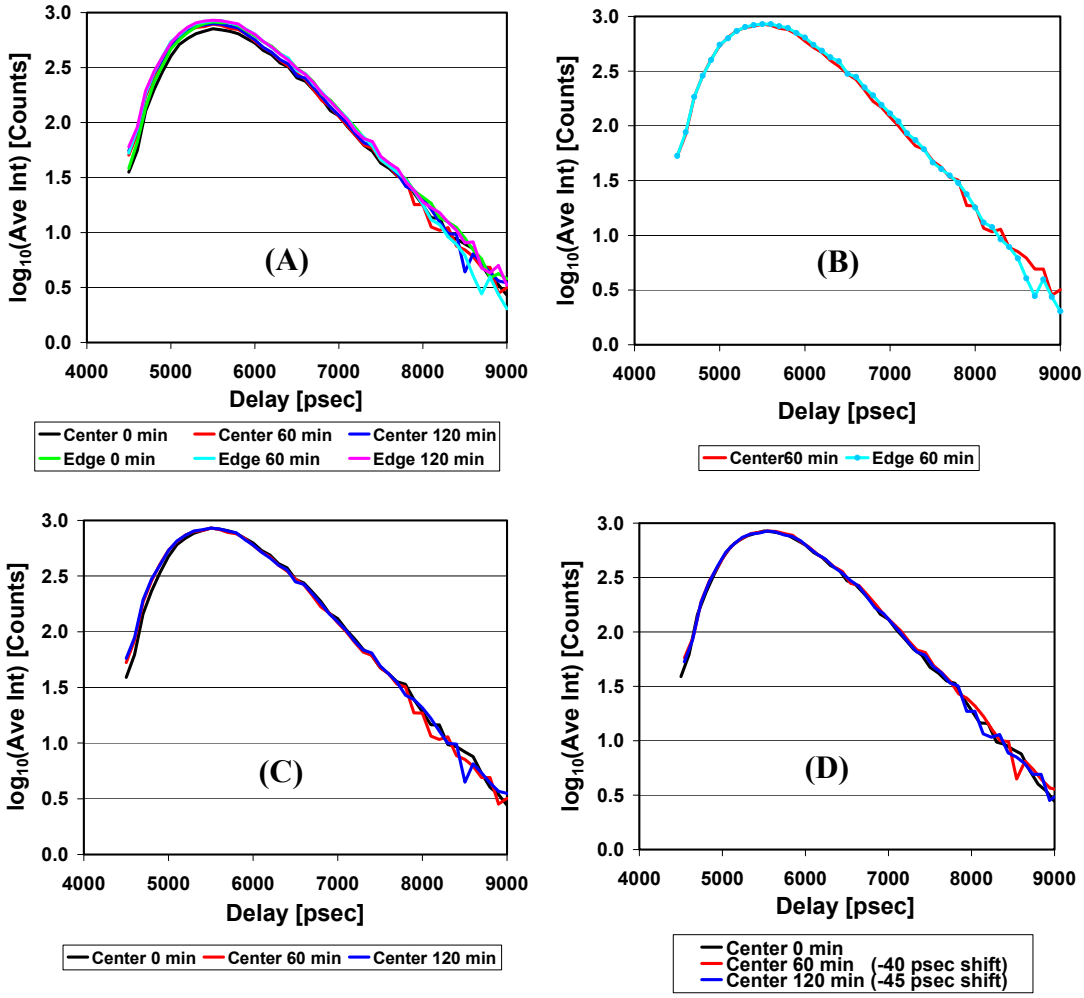

Figure 6.5 Stability with time from system start is shown for TPSF's acquired at 0, 60 and 120 minutes from turn-on of the laser system. The unaltered TPSF's are shown in plot (A), indicating an increase in intensifier response with time. The differences between the 0 and 60 minute TPSF's relative to the 120 min TPSF are shown in plot (C). The shifting of the 60 and 120 min TPSF's to the right by 40 and 45 psec, respectively, results in the overlap of the TPSF's. This shift is likely due to a decrease in fiber and phantom index dn/dT with increasing temperature in the room.

phantom and one at the edge. The magnitude of the peak of the TPSF was observed to increase with warm-up time. Most of the warm-up was within the first hour, but warm-up effects were still observed between the 60 min and 120 min trials. Plot (B) of Figure

6.5 indicates that there was very little difference between the center and edge source fiber TPSF's. The asympotic tail of plot (B) would indicate an increase in absorption for the edge source, but the other cases did not, so it may not be statistically significant, given the low SNR for the long delays. Plots (B), (C), and (D) were shifted in magnitude to make all traces peak at the same magnitude. Plot (C) shows the difference between the 120 minute trace and the first two trials. Trial 3 was taken to approximate the steady state, as no further change with warm-up was noted. The room in which the experiments took place was small and poorly ventilated. The laser produced a significant amount of heat that was dumped into the room, increasing temperature with time. It is likely that the room temperature increased by more than 10 degree Celcius over the period of the test. The change in fiber core (fused silica) index with temperature, dn/dT, is 1.2×10^{-5} per degree Celcius in the near infrared. The total length of the probe fiber bundles is approximately 10 meters. This would be expected to lead to an increased delay on the order of 30 psec between trial 1 and trial 3. Also, the thermal expansion coefficient of fused silica on the order of 5.5×10^{-6} per degree Celsius, would bring this to approximately 45 psec. The observed shift, however, was toward shorter times by 40 psec for the 60 min trial and 45 psec for the 120 min trial. Thus, some other mechanism must be responsible for the shift toward shorter delays with increased warm-up time and temperature. The thermal expansion coefficient of the silicone from which the phantom was made is on the order of 8×10^{-4} per degree Celcius. This would be expected to increase the thickness of the phantom by about 0.5 mm over the temperature range. But again, this would increase the delay, by less than a few psec. A decrease in the density of the phantom due to expansion would be expected to shift the delay in the correct

direction, but would also be expected to increase the width, which did not appear to happen. Thus, the evidence points toward an electronic cause. Two potential electronic causes of the shift would be a change in the response of the delay box or a shift in the output of the laser trigger with temperature. Plot (D) of Figure 6.5 shows that after applying the shifts, the TPSF's all line up. The small difference for the first few time gates is believed to be associated with transient saturation effects that will be explained later in this Chapter.

6.1.3 Transient Response – Wavelength Change and Data Acquisition

There is interest in the spectroscopy of tissue and tissue chromophores and therefore multiple wavelengths must be interrogated. It would be preferable to have a system source with a broad spectrum covering the entire physiological window of interest. In that

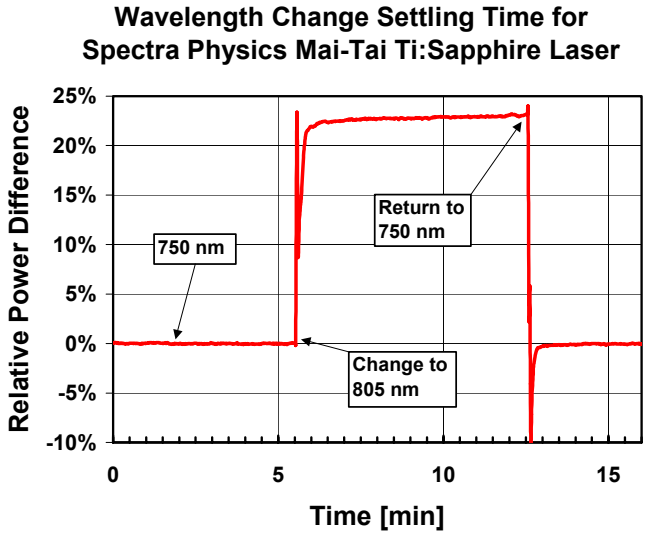

Figure 6.6 The transient response to a wavelength change is shown for the Spectra-Physics Mai-Tai mode-locked laser. The output from one of the source probe fibers was used for this measurement. Note that the response time is shorter for going from 805 to 750 nm than from 750 to 805 nm, indicating a preferred direction for measurement order.

case, spectral separation techniques could be used on the detection side of the system to allow simultaneous measurement of multiple wavelengths. As described above, the laser source has a spectral bandwidth of the order of 10 nm, which necessitates laser source wavelength changes. The Mai-Tai laser changes wavelengths by rotating a grating within the laser cavity to tune over the range of the Ti:Sapphire laser medium, limited to between 750 and 850 nm by the instrument. This mechanical tuning technique requires time and even once the grating is repositioned, time is required to reach a new steady state thermal equilibrium as indicated in Figures 6.6 and 6.7. Most of the change, on the

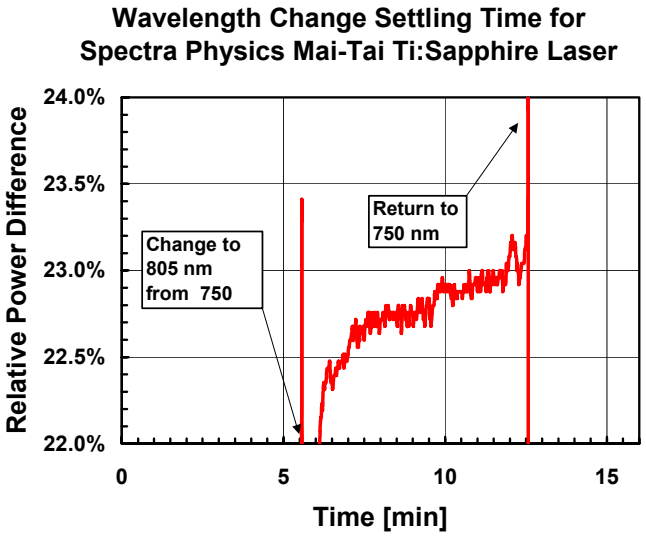

Figure 6.7 The transient response to a wavelength change is shown for the Spectra-Physics Mai-Tai mode-locked laser. The output from one of the source probe fibers was used for this measurement. For a 2-minute measurement window, the laser power changes by the order of 0.25 %, which may necessitate the use of a monitoring photodiode to correct for laser power drift?

order of 23%, is shown to occur within about 15 to 30 seconds in shifting from 750 to 805 nm. Figure 6.7, however, shows a slow drift on the order of 0.5% occurring over the next several minutes. Given that a measurement period for a clinical setting may be limited to the order of 2 minutes, this drift may be acceptable. Even so, if three wavelengths are used for a given measurement, which would require 2 wavelength

changes, a significant portion of the total measurement time budget would be used to equilibrate the system. Thus, it is recommended that for optimization of measurement time, a laser power monitoring photodiode be added to the system. Any noise in the monitoring photodiode will degrade the SNR, so sufficiently low electrical bandwidth and high sensitivity zero biased silicon photodiodes should be used. Another feature to note in Figure 6.7 is that the equilibrium time appears to be shorter in going from higher output (805 nm) to lower output (750 nm), so there is a preferred wavelength order. Interest here, is centered on wavelengths of 760, 805, and 830 nm, governed by hemoglobin absorption spectra. From Figure 6.2, this would suggest that the preferred order would be to start with 805 nm, then shift to 850 nm, and finally to 760 nm. This assumes that the actual time to physically move the grating is not the limiting factor, which is indeed the case, as this occurs within a few seconds.

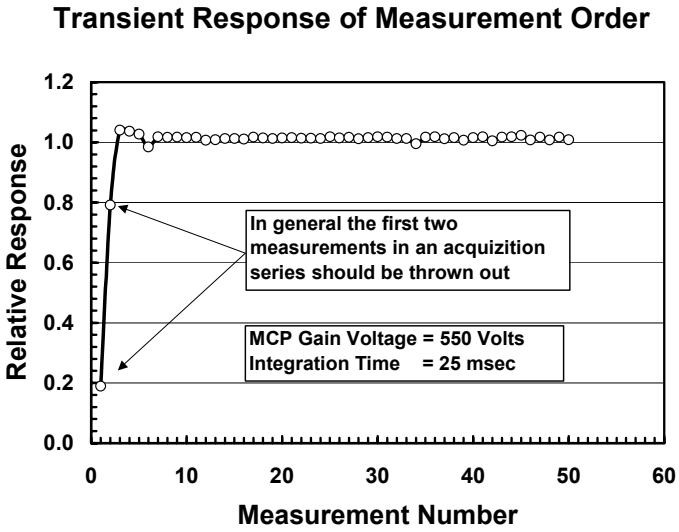

Figure 6.8 The transient response of measurement order is shown, indicating that the first two measurements should be thrown out. I believe that this is a consequence of the settling time for the MCP to go from inhibit mode (low gain) to the operational gain voltage. This problem could be eliminated by use of a fast shutter instead of the gain inhibit.

Figure 6.8 shows another transient response of interest. The plot shows the relative response of a series of image file acquisitions. Each measurement was conducted at the same physical fiber position and should therefore result in the same relative response. The data was collected at a MCP gain voltage of 500 Volts and at an integration time of 25 msec. Data was collected at a range of gain voltages and integration times with similar results. Thus, the first one to two measurements should be thrown out, in general during any measurement series. The nature of this transient response is not understood at this time.

6.1.4 Stability and Repeatability

It is important to understand how stable the measurement system is to assess how much credence to give a particular measurement series. That is, how does one know that if an identical measurement is taken under the same conditions some period of time following the first measurement, that an identical measurement would result, and if not, how different would it be? First, the stability of the laser and multiplexer source subsystems were assessed as a pair for a period of 30 minutes following a 3-hour warm-up as shown in Figure 6.9. The source subsystem appears to be extremely stable to within a standard deviation of less than 0.05% over the 30-minute period with no discernable drift.

A repeatability test was then conducted to assess measurement-to-measurement differences in the relative average intensity from a group of 10 fibers measured at two discrete delay values. The purpose of this test was to answer two questions; 1) How repeatable is the process of revisiting a particular fiber position and 2) How repeatable is the process of switching delays. The complete system was used for this test, including a

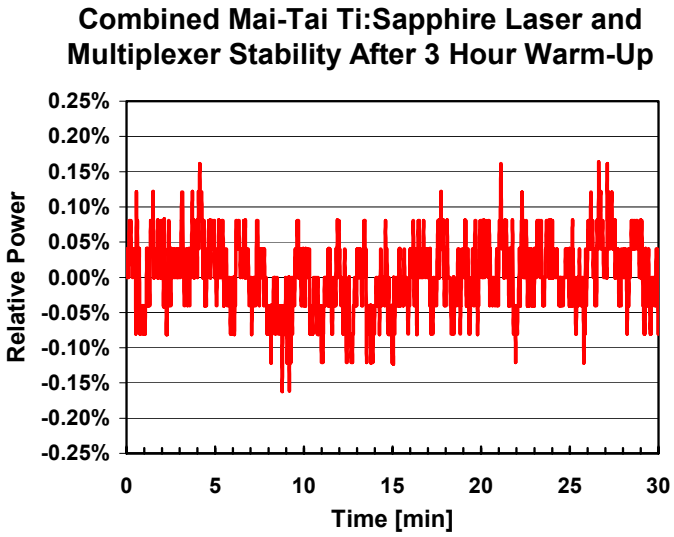

Figure 6.9 The stability of the Spectra-Physics Mai Tai mode locked Ti:Sapphire laser in combination with the fiber multiplexer is shown to be within +/- 0.1% over a 30 minute period following a 3 hour warm up.

homogeneous phantom with background optical properties of $\mu_a = 0.098$ cm^{-1} and $\mu_s' =$ 7.5 cm^{-1}. All measurements were acquired at a MCP gain voltage of 500 Volts and at an integration time of 55 msec. The complete system was allowed a period in excess of three hours to warm up prior to this test. Each data point constituted an average of 50 measurements to allow for determination of the standard deviation. Fifty background images were also acquired for each data point. A 7 by 7 matrix of image file pixels was averaged for each data point (only 4 by 4 are required, but this allowed for some tolerance on locating the center). The complete measurement cycle consisted of first, 10 discrete fiber positions scanned in a serial fashion at the first delay value. This was followed by 10 cycles of these 10 fibers at this first delay. Next, the delay was changed by 25 psec, which was a short enough time that no change in signal level would have been expected. The measurement of the 10 by 10 fibers was then repeated. This two-delay cycle was repeated a total of 10 times comprising the complete repeatability

measurement cycle. The test showed that no resolvable error was introduced by the fiber switching process. The high precision galvanometers were designed to have microradian repeatability, so the results are as expected. Likewise, there was no resolvable error introduced by switching the delay. This result was also expected, as the delays result from physically switching delay lines.

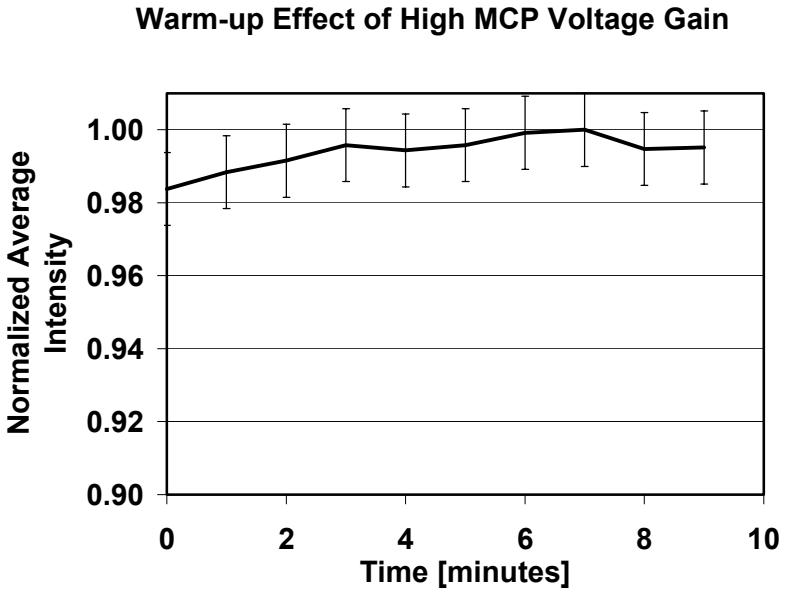

Figure 6.10 The plots show the warm-up due to turning on the high voltage MCP gain on the recorded average intensity. The system had been warmed up for a period of 3 hours prior to this data capture. The MCP voltage is inhibited, except during the actual measurement. The drift may be due to the thermal equilibration of the MCP due to the high voltage during the measurement.

The most important result of the stability test, aside from confirming the stability with fiber and delay switching, was the observation that the high voltage on the MCP resulted in a warm-up phenomenon during the course of a measurement. The warm-up phenomenon is depicted in Figure 6.10, which represents the average response of 10 fiber positions. The system was equilibrated for more than 3 hours prior to data collection. The high voltage was only enabled by the control software during actual data collection. The high voltage could have resulted in heating of the photocathode and MCP structure,

which may account for the drift shown in Figure 6.10. This increased temperature may have increased the number of thermalized electrons in the conduction band, thereby increasing the surface density of available electrons and reducing the surface barrier potential, which would lead to an increased quantum yield. This effect may apply to both the photocathode and the MCP. Thus, there may be another warm-up mechanism that has not been accounted for. One method to alleviate this problem may be to introduce a shutter into the camera system to allow the intensifier to thermally equilibrate prior to a given measurement. The data suggests that this equilibrium time, for the case of 500 volts MCP gain and 25 msec integration time, is on the order of 5 minutes.

6.1.5 ICCD Gain

The gain due to the MCP is shown in Figure 6.11 for the MCP gain range between 400 and 800 volts. The exponent on the fit indicates an effective number of equivalent dynodes of 9.03. Care was taken to avoid saturation effects by acquiring the data at long

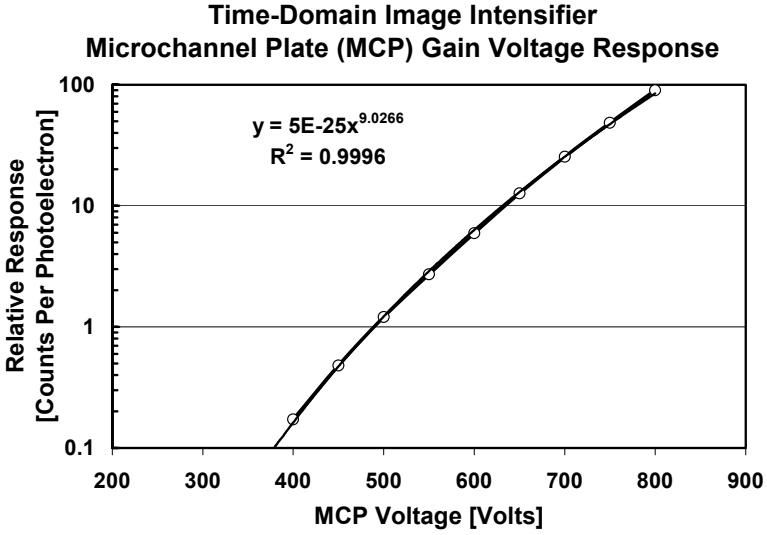

Figure 6.11 The gain response of the ICCD microchannel plate (MCP) is shown as a function of MCP gain voltage. The fit shows an N_{eff} of 9.03, which is indicative of the effective number of interaction sites analogous to photomultiplier tube dynodes. The gain is set to the manufacturer's test data of 90 counts per photoelectron at an MCP gain voltage of 800 volts.

integration times (200 msec) and relatively low count levels. The relative response was set to a value of 90 counts per photoelectron according to the manufacturer's data sheet.

6.1.6 Intensifier and CCD Linearity

There are two basic subsystems to the camera system, the intensifier and the CCD. Both of these components may have regions of operation where the relationship between the magnitude of the incident signal power and the relative output show a nonlinear response.

First, the linearity of the intensifier is addressed. The intensifier has two contributions to nonlinear response as described in Chapter 5. The low MCP gain voltages show saturation due to photocathode electron mobility rate limits, below about 600 Volts MCP gain. The high MCP gain voltages show gain saturation due to the finite strip current in the MCP associated with neutralizing the space charge buildup at the

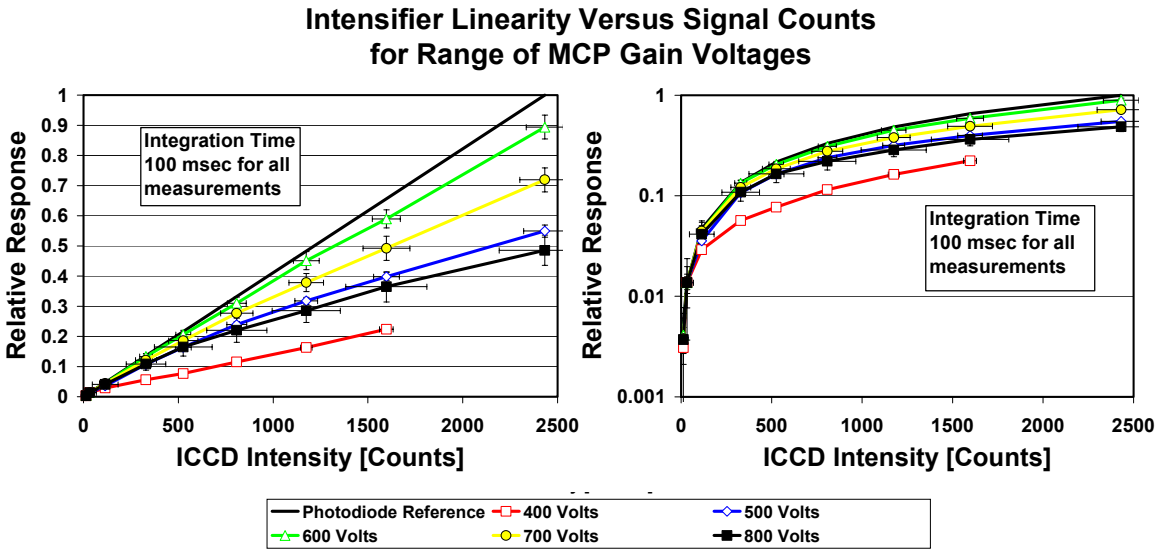

Figure 6.12 The deviation from linearity for the intensifier response to increasing photon flux is shown for a range of MCP gain voltage. All measurements were carried out at an integration time of 100 msec.

proximal end of the device. Figures 6.12, 6.13 and 6.14 represent the nonlinear response of the intensifier. The data was collected at a wavelength of 750 nm through the entire system with the high absorption tissue phantom between the compression plates of the probe. The solid black line represents the linear response of a calibrated low-noise silicon photodiode reference (ThorLabs Model S20MM). Figures 6.12 and 6.13 show significant photocathode saturation for the cases of 400 and 500 Volts. The 600 Volt

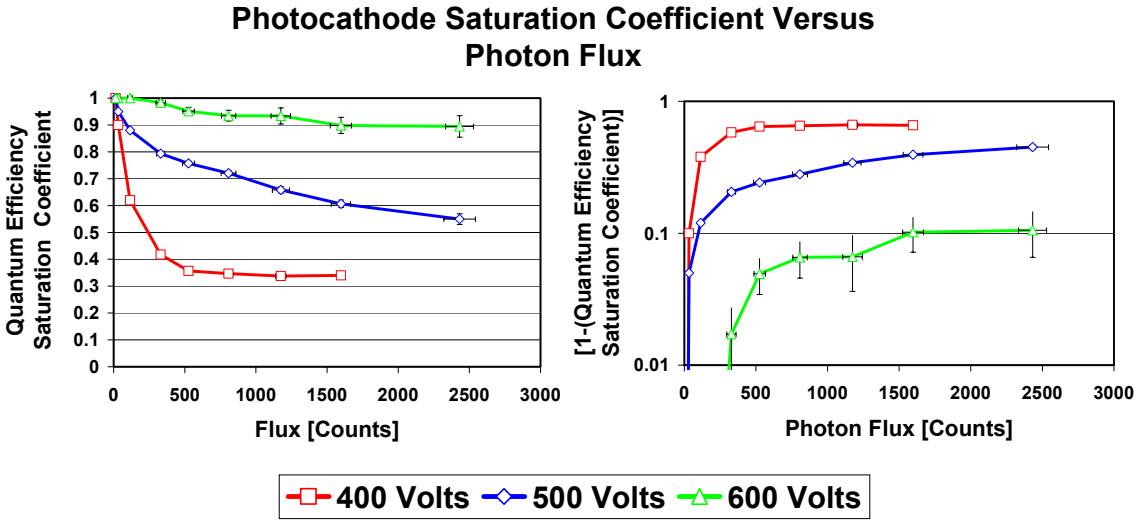

Figure 6.13 The photocathode quantum efficiency saturation coefficient is shown as a function of ICCD counts for 400, 500 and 600 Volts MCP gain voltage. The plot on the right is 1 minus the coefficient to allow visualization of the affect for low counts.

response may be due to a combination of a small degree of both saturation effects, so it may be more correct to decrease the magnitude for the 600 Volt case in both plots, but it is difficult to say which effect dominates, so the full saturation effect is shown in both cases. It is clear that it is desirable to operate the system near 600 Volts if possible. It may be necessary, however, to account for the nonlinear response, even at 600 Volts. Failure to correct for the nonlinear response would result in errors in the shapes of the TPSF's and therefore, errors in the fits to the forward model for image reconstruction. The critical point should be made that the nonlinear response of the intensifier due to

saturation effects, is very much dependent on the specifics of the measurement. That is, the saturation is sensitive to the total integrated flux on the photocathode, not just during the open gate window, but also over the full pulse-to-pulse period. This was determined by conducting CW measurements with a 630 nm LED. Saturation limits were reached at significantly lower average photoelectron generation rates in comparison with a narrow pulse (impulse response) from the laser. Thus for investigators interested in working on small animals, or on systems for which the photons experience a short total mean path relative to that of a breast or breast phantom, the TPSF is relatively narrow, and they might expect to be less susceptible to intensifier nonlinearity. For the case of a breast or breast phantom with a moderate to low absorption coefficient, μ_a on the order of 0.08 to 0.02 cm^{-1} for example, the TPSF would take up a significant portion of the 12.5 psec pulse-to-pulse laser period, for tissue thicknesses of greater than 4 to 5 cm. Thus the higher average powers of a CW system are approached for equivalent count rates and MCP gain voltages and one could expect to have to deal with nonlinearities of the magnitude indicated in the figures. The extent of the nonlinear response would be a function of the MCP gain voltage, delay, gate width, tissue background properties and thickness, laser power, laser repetition rate, ambient background power, number of measurements at a specific source position. Figure 6.13 shows plots of the saturation coefficient for the quantum efficiency, due to photocathode saturation. Again, the 600 Volts gain may have components due to a combination of photocathode and MCP gain saturations. It is also interesting to note how the 400 Volt saturation roles over. This behavior was not atypical of high saturation levels. Figure 6.14 shows the gain saturation that occurs primarily for 700 and 800 Volt MCP gain voltages. Both of these effects will

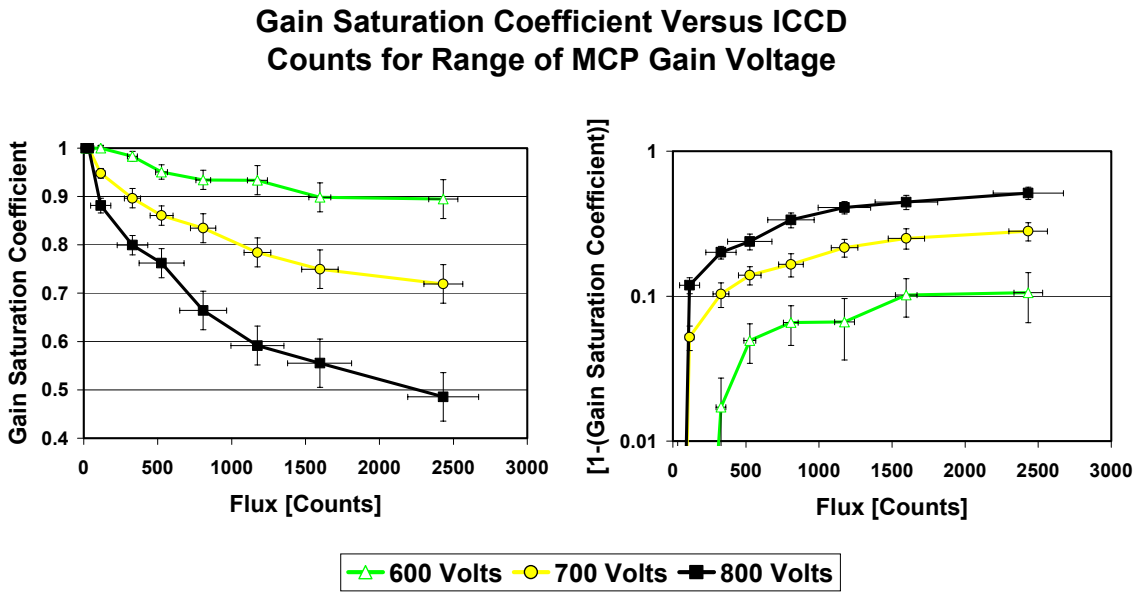

Figure 6.14 The gain saturation coefficient is shown versus ICCD counts for 600, 700 and 800 volts MCP gain voltage. The plot to the left shows 1 minus the coefficient to resolve the response at low counts.

be included in the SNR data fit that is described below. Again, it is emphasized that the saturation effects could be significant and could lead to unacceptable errors if not corrected for. There may be a benefit to operating under saturation conditions, as long as they are accurately measured and accounted for. Saturation increases the magnitude of the low signals relative to those of the high, thereby effectively increasing the dynamic range of the system. Thus the low signals, at fiber detector positions far from the one directly across from the source fiber, would exhibit proportionally higher SNR's than they otherwise would. Perhaps the most significant issue with regard to saturation effects is that they are localized to specific regions of the device. That is to say, the saturation effect that a given microchannel experiences will depend on the signal that came before it. One region of microchannels may experience saturation, where another region may not. This fact may justify stepping through the source fibers in a specific way, such as a standard raster scan. The order of the delays may also be important. Figure 6.15 shows

the transient saturation response of a set of 50 consecutive measurements of the same source and detector fiber positions at an integration time of 50 msec for a range of MCP gain voltage. The dead time between measurements was determined to be 65 msec,

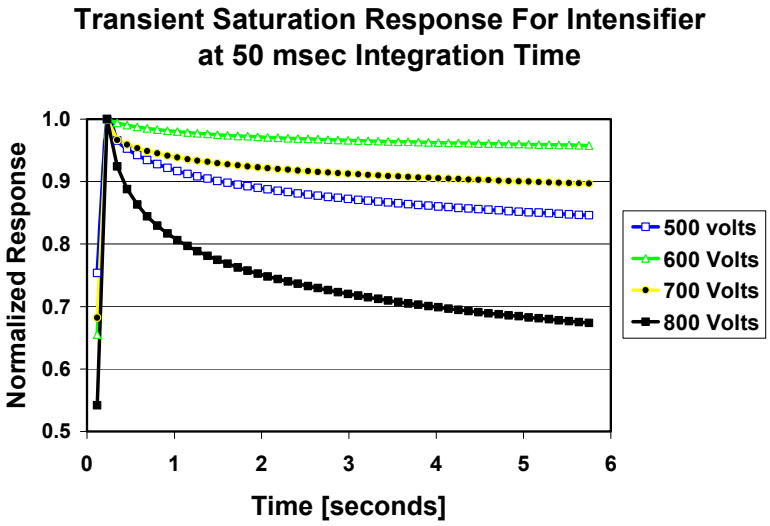

Figure 6.15 The transient response of measurement through a homogeneous phantom at 50 msec integration time at a range of MCP gain voltages is shown. The data represents the best fit to the actual data set.

giving 115 msec between successive measurements. Interpretation of the data of Figure 6.15 would have been complicated by the noise fluctuations, so the data represents the best fit to the actual data, as interest was only on the shape of the curve, not its statistics. Again, it is preferable to operate at 600 Volts MCP gain voltage, if possible. This was, by the way, the recommended gain setting by the manufacturer.

Further examination of any differences between the intensifier saturation observed above and that which might be expected from the scan of a normal breast or breast phantom is warranted, given the magnitude of the saturation effect. In order to achieve good statistics, 50 images were acquired at the same source position. It can be seen from Figure 6.15 that the first few images for each MCP gain voltage have not saturated

appreciably for MCP gain voltages near 600 Volts. If only one image per source position was acquired, the cumulative exposure for a given detector fiber position could be significantly reduced, depending on the background tissue absorption and the order of scanning through the source positions. Low absorption coefficients would result in a greater cumulative exposure over the course of a raster scan and thereby increased saturation. The optimal order of scanning sources would minimize cumulative exposure within the time of a given delay scan. The point here is that the saturation analysis above is likely to be significantly worse than that which would generally be encountered in a normal scan. Thus, it is probable, that for MCP gain voltages on the order of 600 Volts under normal scanning conditions, there may be negligible saturation effects. There is no constant here, as the tissue boundaries for every breast will be different and thus there would need to be an algorithm developed to determine the optimal source scan order for a given breast scan.

The linearity of the ICCD's CCD camera is shown in Figure 6.16. Both the low and medium flux levels were acquired at the same MCP gain voltage of 500 Volts. The third trace indicates that the low and medium flux levels superimpose when scaled to each other, indicating that the nonlinearity for integration times below 25 msec is independent of flux. It was also shown to be independent of MCP gain. The x-intercept of the response is at 12 msec. Therefore, a correction of –12 msec must be applied to the data to insure a zero intercept. The fit to the data for integration times above 25 msec showed a linear response. This linearity was governed by the camera timing, which was extremely precise. The CCD was an interline-transfer chip and does not have a mechanical shutter. The time constant of the P43 phosphor was under 1 msec. No plausible explanation was

developed for this nonlinearity, nor was the manufacturer able to explain it. In general, the system could begin to exhibit appreciable saturation for integration times below 25 msec, so there is limited interested in that region anyway. In general, it is recommended that integration times no less than 25 msec be used.

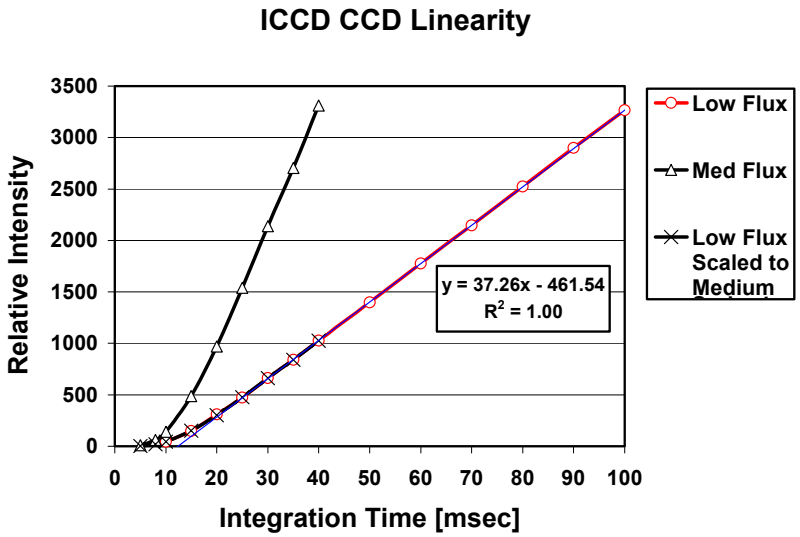

Figure 6.16 The linearity of the LaVision ICCD's Sony CCD camera is shown for two flux levels, both obtained at an MCP gain voltage of 500 volts. The data fit indicates the expected linear response. Non-linear response is observed for integration times less than 25 msec. The intercept of the integration time axis is 12 msec. The low and medium flux levels exhibit identical non-linear response as indicated by the scaled data.

6.1.7 Impulse Response

The impulse response of the system is defined as the TPSF of the complete Time-Domain Breast Imaging System with no bulk scattering medium between the compression plates of the probe. The impulse response is the convolution of the laser pulse with the temporal dispersion effects caused by scattering off optical elements, dispersion within the optical fibers, optical path length variations within the two lens systems, and MCP gate bandwidth. Figure 5.17 shows a plot of the impulse response for an average of 148 source fibers for both with and without compression plates in place. A

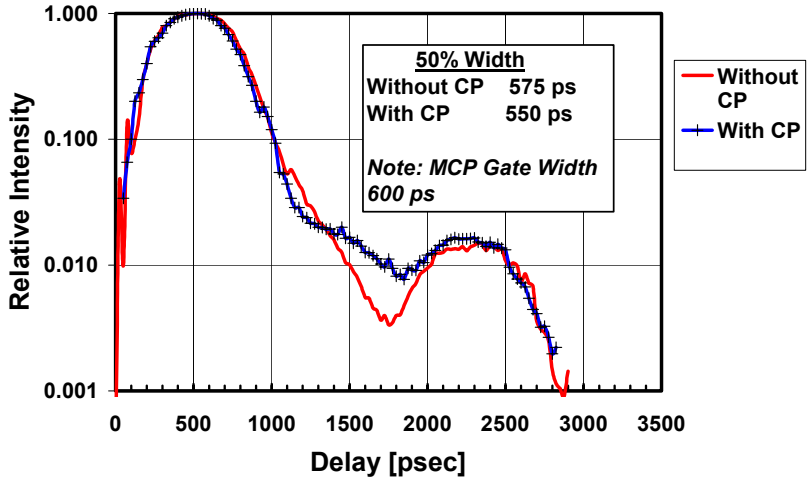

Figure 5.17 The average impulse response for the complete Time-Domain System is shown both with and without compression plates (CP) for 148 source fibers. The standard deviation of leading edge, width, and falling edge are all on order of 25 to 35 psec.

black diffusive sheet of paper was placed over the detector fiber plate to simulate the far field angular distribution of radiation incident on the detector fiber that would be expected with tissue or a tissue phantom. If this were not done, the radiation would under-fill the fibers' and imaging system's numerical apertures, which are 0.39 and 0.22 respectively, which would change the shape of the impulse response. As stated above, the saturation effect was expected to be small for the case of no bulk scattering, in fact it was not resolvable at the 600 Volt gain of this measurement. There are several important points to make regarding the shape of the impulse response. The full-width at half-maximum (FWHM) was found to be 550 psec with the compression plates and 575 psec without them. This is consistent with the setting of 600 psec for the photocathode gate width. The gate was found to be unstable for times less than 600 psec, although the manufacturer claimed that the system was capable of going down to 200 psec. The standard deviation of the FWHM and peak delay was within 25 to 35 psec for all but one

fiber. This was consistent with the manufacturer's specification of 25 psec system jitter. 25 psec would correspond to a 5 mm standard deviation in fiber length, so it is clear that the design goal for fiber length variations was met. The one fiber that fell outside the range, by 100 psec was known to have a different length and was not included in the average. The next feature to notice is the secondary peak at a 1% level approximately 1800 psec following the primary peak. This effect was traced to a retro-reflection of the image of the fiber array off the photocathode, back to the fiber array and then back to the photocathode. This was a consequence of the relatively high reflectivity of photocathode semiconductor material and the properties of a 1:1 imaging system. Light travels 30 cm per nanosecond in air, so the 1800 psec would correspond to an optical path on the order of 16 cm, or approximately twice the length of the 1:1 camera objective. Perhaps the simplest method for minimizing the effect of the reflection would be to use an index matching epoxy to attach a window having the proximal side coated with a high performance anti-reflection multiplayer dielectric stack so as to significantly suppress the ghost reflection causing the secondary impulse response peak. Also, notice a slight difference in the slope of the tail of the primary peak between the two traces. The slope is somewhat reduced for the case of with the compression plate, which may be due to scattering and multiple reflections in the compression plate. In Chapter 4, the compression plate was described as having an anti-reflection coating on both sides, however, such coatings have their limitations and they cannot account for the effects of scratches on the surface and scattering centers within the bulk of the polycarbonate material that comprises the compression plates. A design for a compression plate mask was explored that would allow the entire polycarbonate surface to be covered with flat

black paint except in the regions of the fibers and their fields of view. This would be expected to increase the slope of the tail as to be indistinguishable from that of the case with no compression plates, if deemed necessary.

6.1.8 Cross Talk

The cross talk between adjacent detection fibers was investigated by covering all but one central fiber in the detection probe array with aluminum foil to assure that only one fiber was illuminated. A sheet of black construction paper was placed over the fiber to attenuate the signal and to assure proper far-field filling of its numerical aperture. Cross talk refers to signal that is coupled into a non-illuminated fiber adjacent to an illuminated one. The tolerance to cross talk is dependent on the probe configuration. If for example, one did not take care to assure that fiber positions far apart on the detection probe array

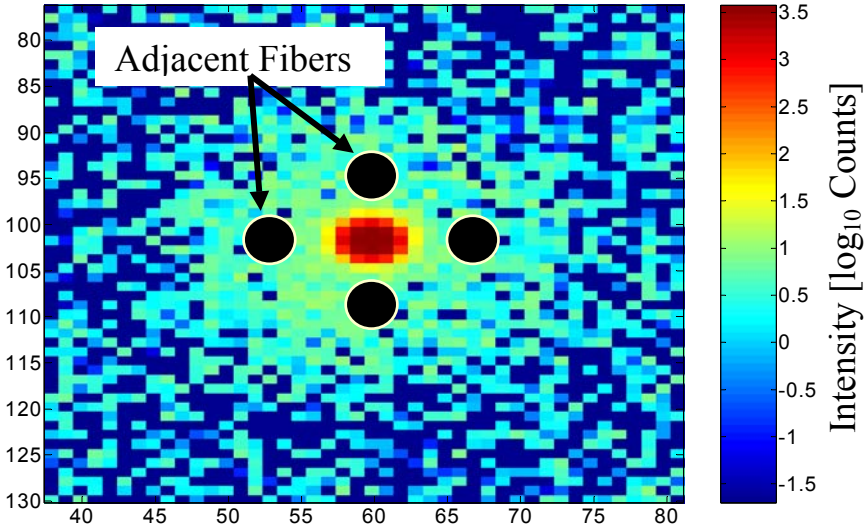

Figure 6.18 The cross talk is shown for the case of a single fiber exposed to source flux. The positions of the adjacent fibers are indicated by the black circles, indicating that the signal level is attenuated by 3 orders of magnitude. This is excellent performance for this probe geometry.

were not adjacent to each other on the image of the detection fiber array mapped onto the photocathode, large errors in the low signal fiber could result. A point was made to maintain a high level of 1-to-1 mapping between the probe-end and camera-end of the detection fiber array. Thus, a low signal would not be expected to be adjacent to a high signal, given the system geometry and background optical properties. If, however, future researchers are interested in reflection probe geometries, cross talk could be more of a concern. Figure 6.18 shows that the cross talk signal in adjacent fibers, represented by the black circles, was down by just over three orders of magnitude from the peak value of the illuminated fiber. This was excellent performance for this system configuration. The primary cause of cross talk at these pixel distances may have been due to scattering within the optical system. Recall that the fiber NA is 0.39 in comparison to the lens system NA of 0.22. Thus, the square of this ratio, or 314% more radiation entered the system than was necessary, as only the radiation within the lens system's NA was imaged onto the photocathode. This was confirmation of the good performance of the custom radiation trap surrounding the central lens elements.

6.1.9 Dark Performance of ICCD

A great deal can be learned about how a given detection system works by investigating its dark performance. The probe fiber array was removed from the front of the ICCD's fiber array imaging lens interface and covered with aluminum foil to assure that no ambient light could leak to the photocathode. The room lights were turned off as a further precaution. The results are shown in Figure 6.19. Plot (A) shows the average dark signal from the ICCD as a function of integration time for a range of MCP gain voltage

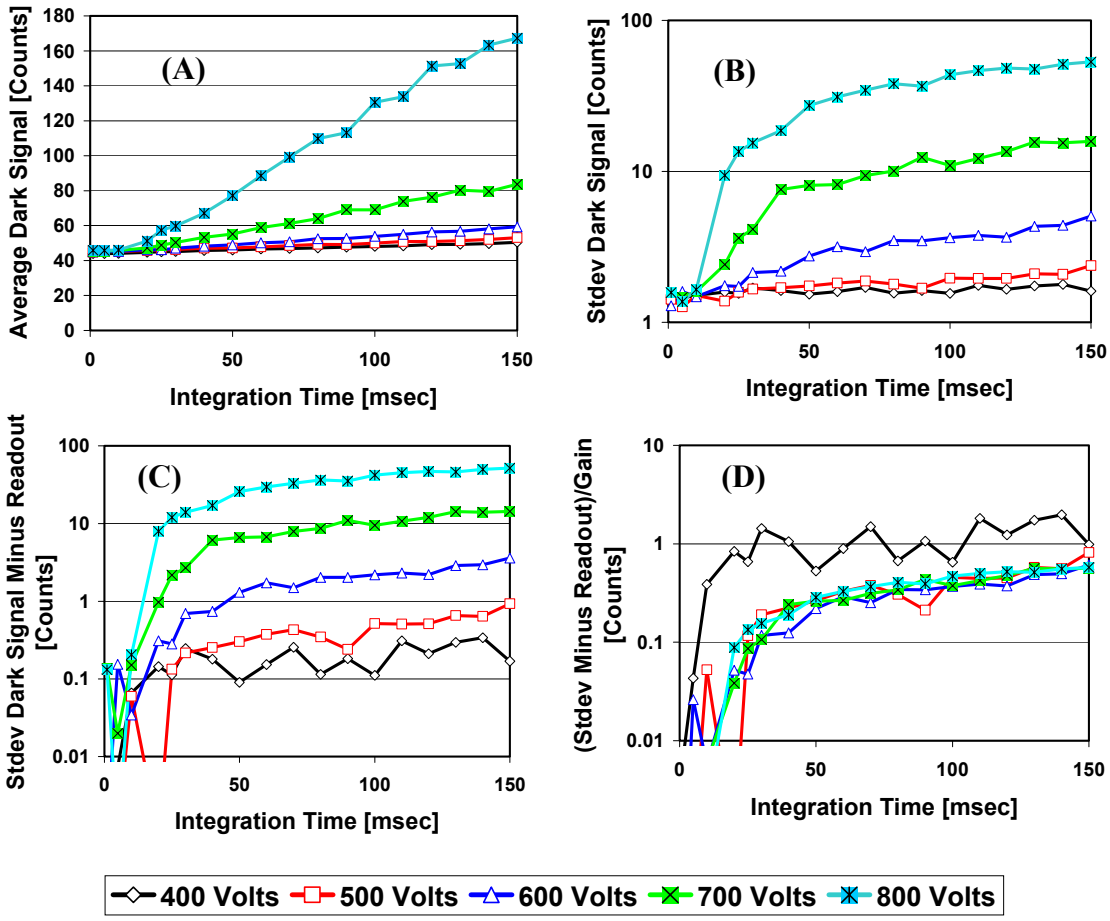

Figure 6.19 Plot (A) shows the average dark signal (objective lens covered) from the ICCD as a function of integration time for a range of MCP gain voltage between 400 and 800 Volts. The increased signal with integration time is due to the combination of thermionic emission from the photocathode and dark signal from the CCD, which both scale linearly with integration time. The standard deviation of the dark signal is shown in plot (B). Plot (C) shows the standard deviation with the readout noise subtracted off (the integration time independent signal that can be quantified for integration times under 10 msec). Plot (D) shows the result of dividing plot (C) by the gain. The excess noise factor is observed for the case of 400 Volts MCP gain voltage.

between 400 and 800 Volts. The increased signal with integration time was due to the combination of thermionic emission from the photocathode and dark signal from the CCD, which both scaled linearly with integration time. The standard deviation of the dark signal is shown in plot (B). Plot (C) shows the standard deviation with the readout noise subtracted off. The readout noise was determined by noticing that readout noise was independent of integration time and therefore, the integration times below about 10

msec give a good estimate of the magnitude of the readout noise. Plot (D) shows the result of dividing plot (C) by the gain. Notice that when divided by the gain, all but the 400 Volt gains are superimposed. The increase in noise for the 400 Volt MCP gain was a manifestation of the excess noise on the equivalent amplified thermionic emission signal power. There are a few more points worth mention. With reference to plot (A), there was a background on the order of 45 counts that must be subtracted from the data to prevent nonlinear response. It would be wise to acquire some statistically sound number of background images, perhaps 5 to 30 depending on the drive conditions, to minimize degradation of the SNR through the background subtraction process. In addition, notice that the increase in dark signal is not that substantial for MCP gain voltages of 600 Volts and below. For the case of both 700 and 800 Volts, the dark signal, primarily due to thermionic emission at the photocathode, becomes appreciable. This can confound signal processing and thus, the recommendation is made that other investigators use 600 Volts gain when possible for yet another reason. The thermionic emission will be shown not to have a substantial effect on the SNR, but it could create problems in the case of small data sets. For example, at 800 Volts MCP gain, the total ICCD gain was on the order of 200 counts per photoelectron, thus one thermionic emission result could have a negative impact on a given data series, unless averaging was accomplished over a greater number of pixels. It would be advisable to use the water-cooling option on the camera, if available, to reduce the effect of thermionic emission.

6.2 Comparison of Theoretical and Measured SNR Data

This chapter concludes with a comparison between the SNR theory presented in Chapter 5 and measured data. All data was measured with the complete system using the

high absorption phantom described previously. In order to obtain the appropriate signal levels over the range of MCP gains between 400 and 800 Volts, a combination of polarizer angle adjustment and the addition of black sheets in front of the detection array of the probe were used. In order to obtain repeatable steps in the signal flux, in the case of evaluating SNR versus signal flux, the galvanometer was positioned to step across the input source fiber. The repeatability of this approach was demonstrated by use of a reference photodiode and was shown to be better than 0.1% in standard deviation. The integration time for the case of SNR versus signal photon flux was 100 msec for all MCP gain voltages. The maximum average count of a given measurement was set by adjusting the attenuation level by rotation of the polarizer for each measurement. The high standard deviation for high MCP gain voltages could cause some spread in the mean intensities from measurement to measurement. Each data point on the plots of Figure 6.21 represents the mean value of a set of 50 independent measurements of the source intensity and 50 measurements of the background to allow for good statistics for both the average signal and subtraction of the background. Each of the 50 data points represents the mean value of a 4 by 4 array of pixels on the raw image file. The transient response shown in Figure 6.16 was factored out of the data, so as not to artificially increase the standard deviation and depress the SNR. The same four parameters were explored here as were presented in the theoretical predictions presented in Chapter 5. These include; (1) SNR versus integration time and (2) signal photon flux, both at a range of MCP gain voltage between 400 and 800 Volts, (3) SNR versus MCP gain voltage for a range of integration times between 25 and 200 msec, and (4) SNR versus integration time for the

case of constant integrated signal photons for a range of MCP gain voltage between 500 and 800 Volts. The SNR Equation 30 of Chapter 5 is repeated here for reference.

$$SNR_{ICCD} = \frac{\frac{\eta_{pc}\varepsilon_{(P_s)}\Omega\Gamma P_s\tau}{h\nu} G_{MCP(P_s,V)} G_{Phos}\varepsilon_{relay}\eta_{CCD}\left(F_{SPSF}F_{bin}\right)}{\left[\left(\eta_{pc}\varepsilon_{(P_s)}\Omega\Gamma\frac{\left(P_s+P_B+P_{D(\mathrm{int})}\right)\tau}{h\nu}\right)\left[\left(G_{MCP(P_s,V)}G_{Phos}\varepsilon_{relay}\eta_{CCD}\gamma\right)^2+\left(G_{MCP(P_s,V)}G_{Phos}\varepsilon_{relay}\eta_{CCD}\gamma\right)\right]+\left(\frac{\eta_{CCD}P_{D(CCD)}\tau}{h\nu_{phos}}\right)+\left(\frac{\Delta n_{rms(readout)}}{n_{CCD}m_{CCD}}\right)^2\right]^{1/2}} \quad (5.31)$$

It is not possible to distinguish between the effects of the background power and dark power of the photocathode according to Equation 5.31. The dark power on the photocathode was measured at high gain with the photocathode blocked from outside photon flux. Thus, the magnitude of the background could be uniquely fit. Also, the lights were turned off and the experiment was covered with several layers of black cloth to assure background levels from the probe were negligible. This only leaves the uncertainty of the background power due to scattering off the camera objective, which was found to be negligible through fitting and cross talk measurements. The saturation effects were divided into those that enter Equation 5.31 as the coefficient of reduction for the quantum efficiency (MCP gain voltages below 600 Volts) and those that enter as a reduction in the MCP gain (above 600 Volts). The data of the figures in Section 6.1.6 were used, as they were derived from the same experiment. An open-area ratio Ω of 0.60 was used, as this is typical according to the literature and the exact value was not available from the manufacturer. A quantum efficiency η_{ph} of 0.04 was assumed. The duty cycle factor Γ of 0.048 was used. The CCD detector quantum efficiency was set to 0.70. The on-chip binning was set to 8 by 8 to agree with the settings on the camera and a post detection binning of 4 by 4 was used, consistent with the system geometry. The readout noise, which was independent of gain and integration time, was measured to be

1.5 counts, corresponding to 3 photoelectrons on the CCD. The peak wavelength of the phosphor was set to 550 nm in the green spectrum. The phosphor gain was taken to be 200 photons/photoelectron and the relay efficiency was taken as 5%. The source fluctuations from the laser and Multiplexer were assumed to have no effect on the SNR. The fit parameters included the signal power, ICCD gain, excess noise factor, number of noise-correlated pixels, the residual background power from scattering within the lens system, and the equivalent dark power on the CCD. The fit parameters are summarized

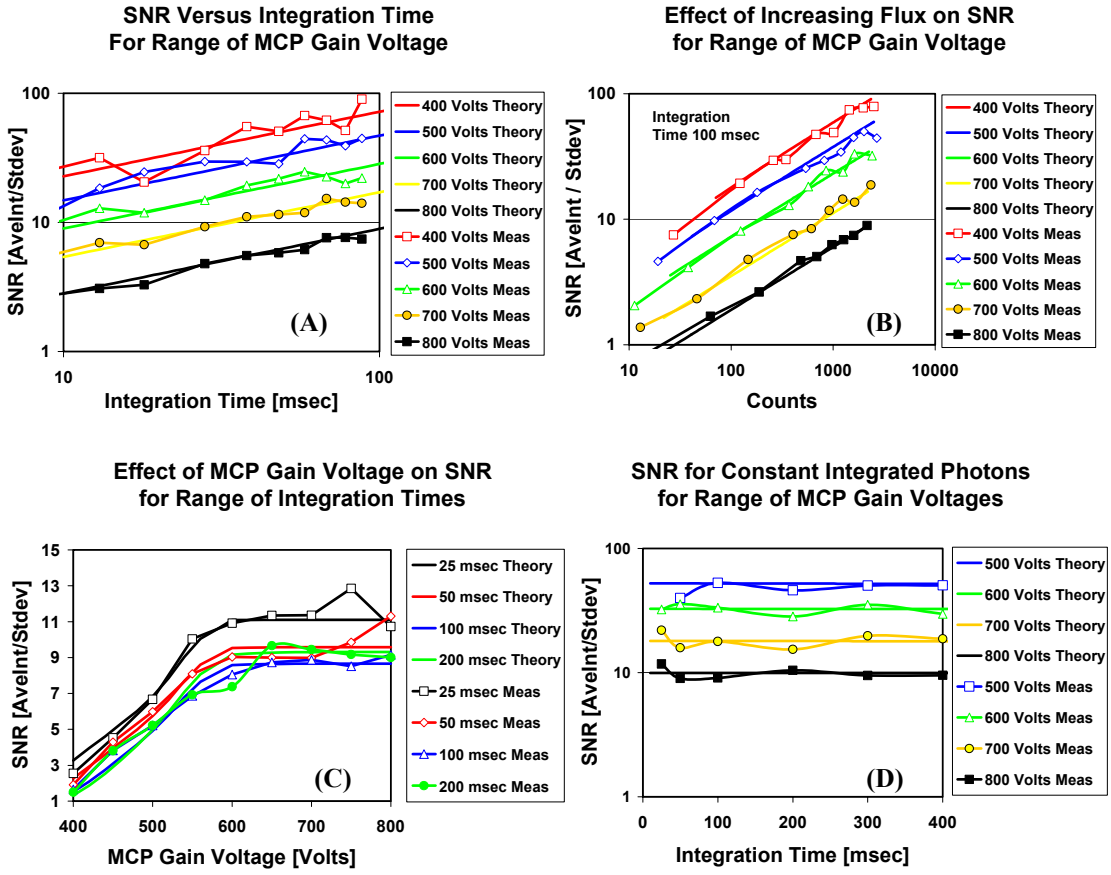

Figure 6.20 Measured data is compared to theoretical data for the case of SNR versus integration time, signal flux, MCP gain voltage, and constant integrated signal photons for a range of MCP gain voltages and integration times as noted. The compression of SNR for the lower voltages is due to the photocathode saturation affects. Gain saturation affects are also accounted for. The excess noise factor was found to be 2.4 at 400 Volts gain and 1.4 at 500 Volts gain. The equivalent CCD dark power was found to be 4.0 E-18 W. The equivalent dark power on the photocathode was found to be 1E-19 W from measured data. The background power on the photocathode was fit to be < 1E-20 W. The readout noise was measured to be 1.5 counts.

in Table 6.1, below. The fit represents the simultaneous minimization of differences between the theory and measured data. The relative ICCD counts of the model were adjusted to agree with those of the data. This is most obvious in the lower left plot C of Figure 6.20 where significant vertical separation would not be expected between the different integration times as discussed in Chapter 5. The separation is almost entirely due to the differences in measured average intensity. The compression of the lower MCP gain voltages is due to the saturation effects. The photocathode saturation has a much more significant effect on the SNR relative to the MCP saturation of the higher MCP gain voltages, as it decreases the number of photons, thereby directly increasing the standard deviation. The slope of the measured data for plot (A) was not in agreement with the theory prior to correcting for the x-intercept by 12 msec as described above. After the correction, good agreement was found with the theory, suggesting that such an offset correction of the integration time is indeed required. The low flux levels at low MCP gain voltages for plot (B) and the low MCP gain voltages of plot (C) were sensitive to the magnitude of the CCD dark power and provided a fit of 4×10^{-18} W, corresponding to 8 electrons per pixel per second. This is high relative to the 0.2 electrons per pixel per second specified by the manufacturer. The system, however, was mounted in its cabinet at the time of these measurements and was subject to overheating. In fact, the system shut down several times during the course of the measurements due to surpassing overheating alarm limits. The dark power of the photocathode was not a problem at this temperature, but it is apparent that the thermoelectric cooler on the CCD was out of operational range, which resulted in a high dark count for the CCD. It is possible to distinguish between readout noise and CCD dark power, as the former is not affected by integration time

while the later is. In plot (D), from the theory, a decrease in the SNR would be expected for short integration times due to saturation effects at the 500 Volt MCP gain voltage. It does not show up here, however, because the measurement compensated for this effect by increasing the average count back to the 2400 count level. Thus, the expected reduction in photon statistics was compensated for. The fit to the excess noise factor is shown in Figure 6.21 to have a knee in the range of 550 Volts MCP gain voltage. This relatively

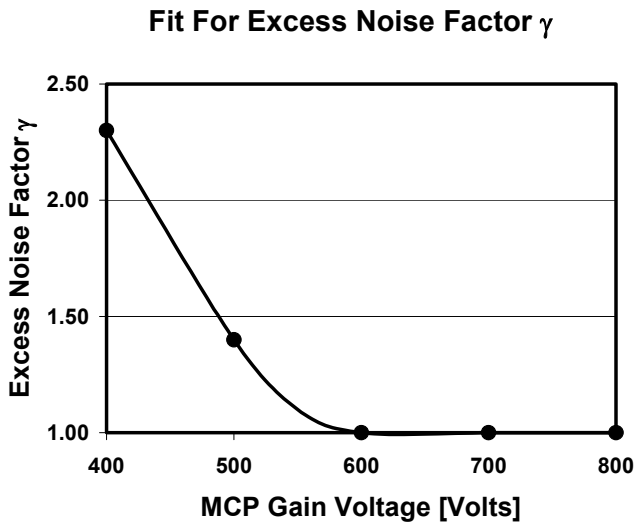

Figure 6.21 The excess noise factor fit to the measured SNR data is shown for a range of MCP gain voltage between 400 and 800 volts.

high excess gain factor is an indication that the secondary emission levels are relatively low for these intensifier systems. This is yet another reason for operating near or above 600 Volts MCP gain voltage. The fit for the reduction in quantum efficiency due to photocathode saturation is shown in Figure 6.22. The fit of 227 counts per photoelectron for the ICCD gain at 800 Volts was in good agreement with that determined by dark thermionic emission observed at 800 Volts MCP gain voltage under dark conditions. The signal power required to produce approximately 2400 counts at 600 Volts MCP gain voltage was shown to be 2.0 $x10^{-16}$ W per microchannel (10 μm diameter), which puts the

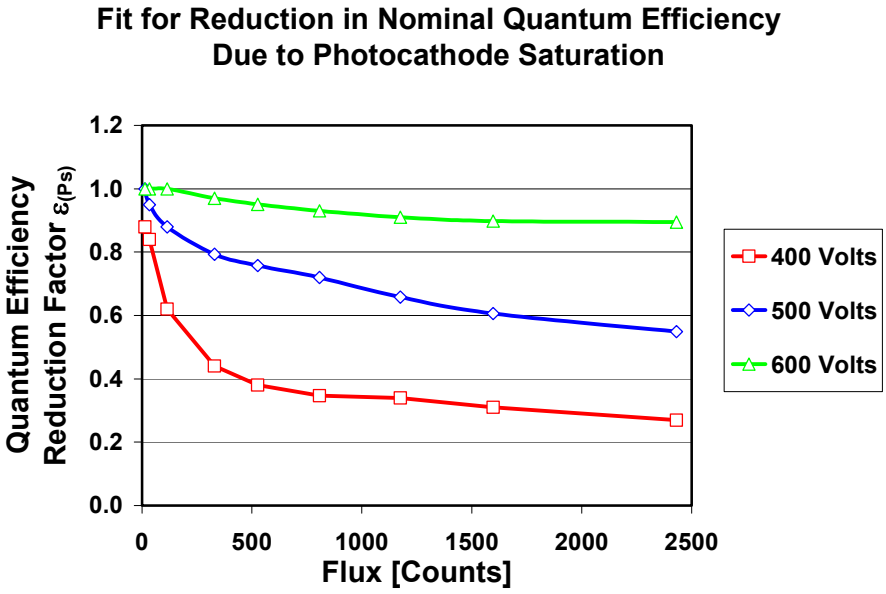

Figure 6.22 The fit for the reduction in quantum efficiency $\varepsilon_{(Ps)}$ is shown for MCP gate voltages ranging from 400 to 600 Volts.

other noise powers in perspective. Also, notice that the number of noise-correlated pixels was found to be on the order of 2, which seems reasonable, given the spread of the SPSF within the MCP. This results in a reduction of the expected SNR to 25% of what one would expect from 8 by 8 on-chip binning.

An additional message that can be derived from the measured data is that the system is limited primarily by photon statistics, as one would hope. This is particularly clear from plot (D) of Figure 6.20.

Parameter	Value	Comment
$P_{D(CCD)}$	4×10^{-18} W	Fit to < 8 e^- /pixel/sec
P_B	$< 1 \times 10^{-20}$ W	Fit
$P_{D(Int)}$	1×10^{-19} W	From measured data
$\Delta n_{rms(readout)}$	1.5 counts	From measured data
P_s (600 V)	2×10^{-16} W	Fit
n_{CCD}' and m_{CCD}'	2	
ICCD gain	227 counts/photoelectron	@ 800 Volts

Table 6.1 Measured and fit data is shown that was used for the fit of measured data to the theory.

6.3 Summary

A detailed and comprehensive characterization of the Time-Domain Optical Breast Imaging System was presented in Section 6.1. One of the most critical points that all investigators must keep in mind is that saturation effects can be significant and must be accurately accounted for in order to get a good fit to the forward model. Care should be exercised not to mistake the saturation data presented as a calibration, as the degree of saturation is affected by numerous parameters. Therefore, one must be sure to characterize saturation for one's specific measurement geometry and parameters.

In Section 6.2, measured data was compared with the theory of Chapter 5. The fit to this data allowed for further characterization of system parameters and performance. The saturation effects accounted for a decreased SNR for MCP gain voltages below 600 Volts. The data also confirmed that the camera system is operating near the photon noise limit for high-count rates. Low count rates begin to be limited by readout noise from the CCD. Overall, this system is well suited to time-domain breast imaging, assuming proper account of saturation effects.